Supplementary Information

for

Directly Measuring Flexoelectric Coefficients μ₁₁ of the van der Waals Materials

Menghan Deng,[1] Xiang Wang,[1] Xionghu Xu,[1] Anyang Cui, *[1] Kai Jiang,[1] Jinzhong Zhang,[1] Liangqing Zhu,[1] Liyan Shang,[1] Yawei Li,[1] Zhigao Hu,*[1,2] and Junhao Chu[1,2]

[1] Technical Center for Multifunctional Magneto-Optical Spectroscopy (Shanghai), Engineering Research Center of Nanophotonics Advanced Instrument (Ministry of Education), Department of Materials, School of Physics and Electronic Science, East China Normal University, Shanghai 200241, China

[2] Collaborative Innovation Center of Extreme Optics, Shanxi University, Taiyuan, Shanxi 030006, China

* Author to whom correspondence should be addressed.
Tel.: +86-21-54342933. Fax: +86-21-54345150.
Electronic mail: aycui@phy.ecnu.edu.cn, zghu@ee.ecnu.edu.cn

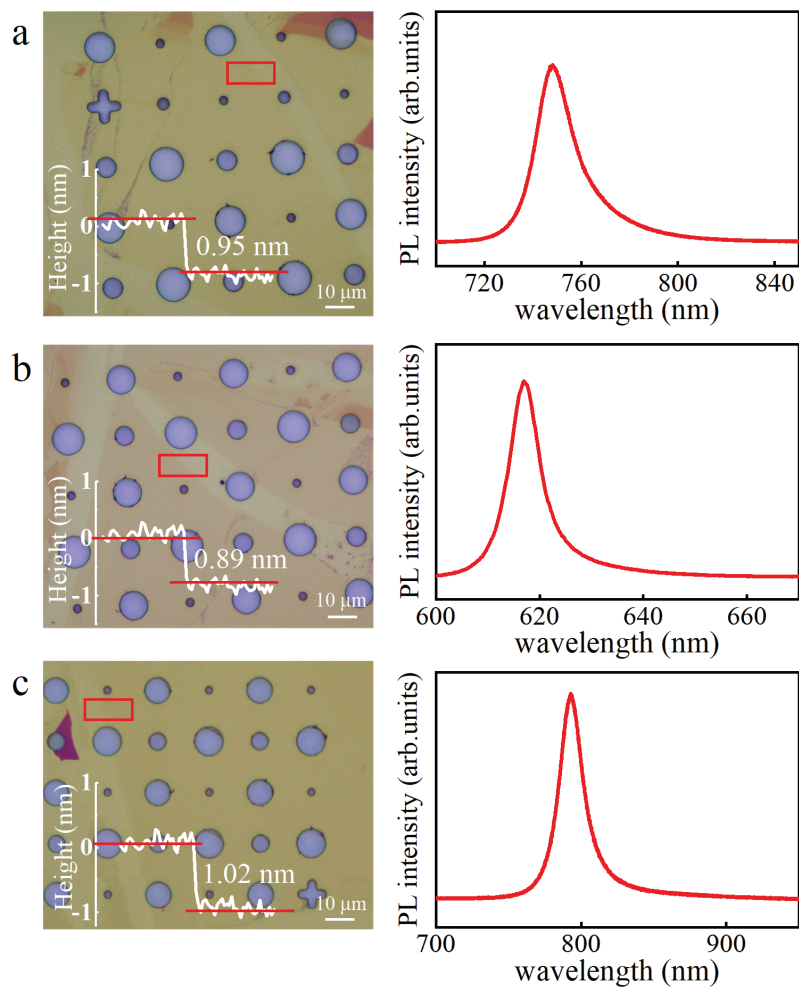**Supplementary Note 1: Nonuniform strain quantification of bent monolayer MX$_2$ (M = Mo, W; X = S, Se)**

Figure S1 | Basic microscopic and photoluminescence spectral characterizations of monolayer MX$_2$ (M = Mo, W; X = S, Se) flakes. The optical microscopy images and typical Raman spectra of **(a)** WSe$_2$, **(b)** WS$_2$, and **(c)** MoSe$_2$ films on the porous substrate. Height profile along the red box is shown in the inset of the left optical map.
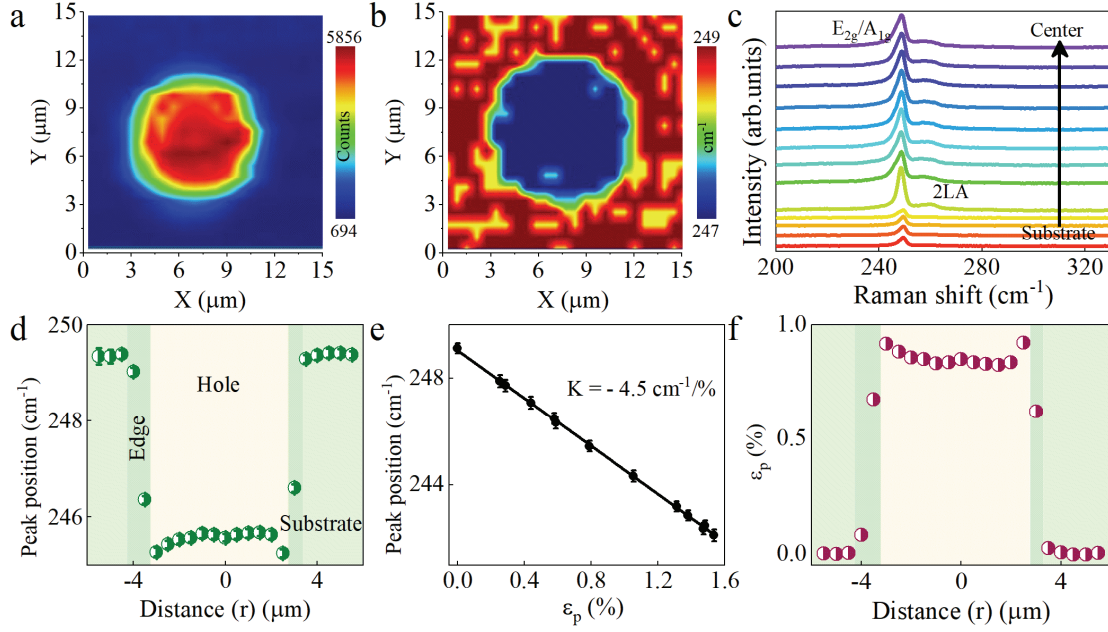
Figure S2 | The Raman spectroscopy measurements of monolayer bent WSe₂ membranes. The E_{2g}/A_{1g} Raman mode **(a)** intensity and **(b)** peak position mapping images of a suspended monolayer WSe₂. **(c)** A series of Raman spectra from the center to the substrate along diameter of hole. **(d)** Raman peak positions of E_{2g}/A_{1g} mode as functions of r. **(e)** Raman peak position of E_{2g}/A_{1g} as a function of biaxial strain. The black solid line is obtained by the least square fitting, and the fitted slope is K = - 4.5 cm^{-1} /%. **(f)** The strain distribution as functions of r.

For the unstrained monolayer WSe₂ film, Raman spectra present two characteristic peaks of the 2LA mode around 260 cm^{-1}, and the E_{2g}/A_{1g} mode around 250 cm^{-1}. [1] Because E_{2g} and A_{1g} modes entangle with each other and are difficult to be distinguished, we define the degenerate peak at 250 cm^{-1} as E_{2g}/A_{1g}. Taking the monolayer WSe₂ membrane with the bending depth of 243.23 nm (the hole diameter is 3.2 μm) as an example, the distribution of strain along the hole diameter was presented. FigureS2a-b display the intensity and peak position mapping images around the bands of E_{2g}/A_{1g} mode. Compared with flat areas, Raman intensity at the curved area is larger, which is consistent with the intensity mapping images of monolayer MoS₂. Similarly, the existence of local non-uniform strain induced an obvious peak shift between the deformed and flat WSe₂ regions. The E_{2g}/A_{1g} phonon softens continuously from the edge to the center, indicating that the local strain continuously varies. A series of Raman spectra from the center to the edge along diameter of hole are shown in Figure S2c. The E_{2g}/A_{1g} mode presents a blue shift trend. In order to present the variation of E_{2g}/A_{1g} mode more intuitively, we extracted Raman frequency (peak position) of E_{2g}/A_{1g} as a function of r, as shown in Figure S2d. The center of bent WSe₂ flakes is defined as r = 0. For the E_{2g}/A_{1g} phonon that is sensitive to the radial strain component, there is a nonlinear trend of firstly increase and then decrease from edge to center. In order to further present the strain distribution of monolayer WSe₂ film, the shift rate of E_{2g}/A_{1g} Raman mode with total in-plane strain was measured. For WSe₂, the value of $f(v)$ is 0.736. Thus, the total in-plane strain could be expressed as $\varepsilon_p^{bottom} = 1.472(\frac{H_{max}}{R})^2$. Raman spectra at the center of monolayer WSe₂ flakes with diverse diameters and the different bending depths were measured.

Figure S2e presents the peak position of E_{2g}/A_{1g} modes as a function of the total in-plane strain (ε_p). The peak position of the degenerate mode shifted linearly with strain at a rate of - 4.5 cm^{-1}/%. According to the shift rate of peak position of E_{2g}/A_{1g} mode with strain, the total in-plane strain distribution along hole diameter in Figure S2f could be obtained. The total in-plane strain firstly decreases and then increases nonlinearly from edge to center, presenting a central-symmetric distribution.
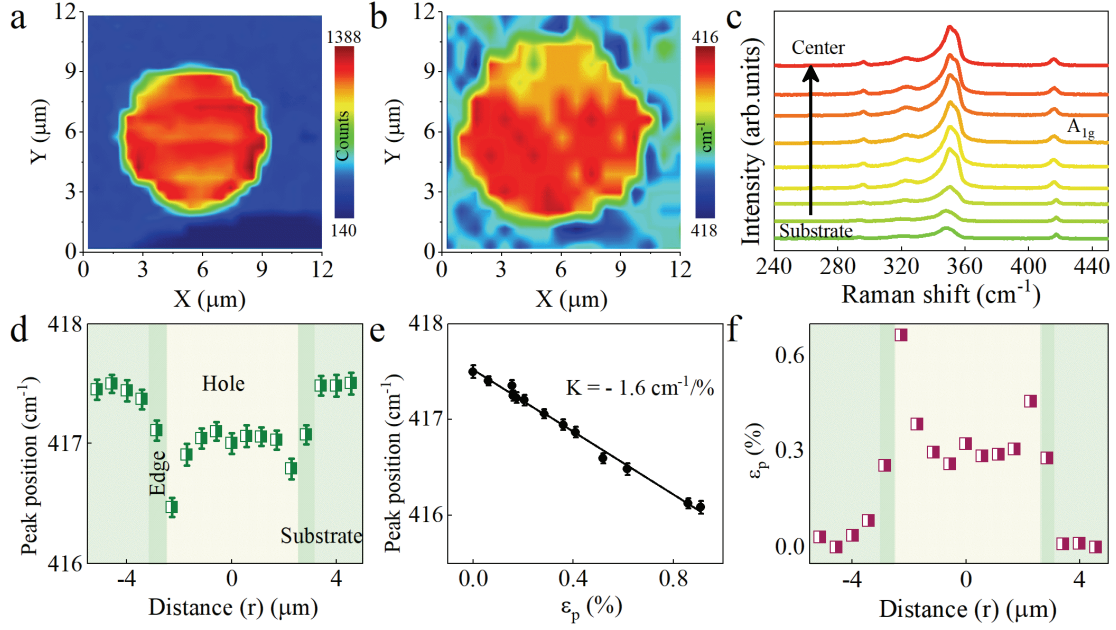
Figure S3 | The Raman spectroscopy measurements of monolayer deformed WS$_2$ membranes. The A$_{1g}$ Raman mode **(a)** intensity and **(b)** peak position mapping images of a suspended monolayer WS$_2$. **(c)** A set of Raman spectra from the center to the substrate along diameter of hole. **(d)** Raman peak positions of A$_{1g}$ mode as functions of r. **(e)** Raman peak position of A$_{1g}$ as a function of biaxial strain. The black solid line is obtained by the least square fitting, and the fitted slope is K = - 1.6 cm^{-1} /%. **(f)** The strain distribution as functions of r.

Raman spectra of monolayer WS$_2$ films present two main characteristic peaks. The prominent broad peak near 350 cm^{-1} is a combination of the threefold degenerate E$_{2g}$ (Γ) mode, E$_{2g}$ (M) mode and 2LA mode. Among them, the first-order E$_{2g}$ (Γ) phonon, the second-order E$_{2g}$ (M) phonon and the second-order longitudinal acoustic phonon 2LA (M) are located at 355.4 cm^{-1}, 343.1 cm^{-1} and 350.8 cm^{-1}, respectively. [2] In addition, the first-order A$_{1g}$ (Γ) phonon is well separated from the other modes and is located at 417.5 cm^{-1}. Taking the monolayer WS$_2$ membrane with the bending depth of 162.45 nm (the hole diameter is 3.4 μm) as an example, the distribution of strain along the hole diameter was presented. Figure S3a-b display the intensity and peak position mapping images around the bands of A$_{1g}$ mode. Similarly, Raman intensity at the curved area is larger than that at flat regions. The existence of local non-uniform strain induces the A$_{1g}$ phonon to soften continuously from the edge to the center. Figure S3c presents Raman spectra of WS$_2$ flakes from substrate to center. We extracted Raman frequency (peak position) of A$_{1g}$ as a function of r, as shown in Figure S3d. For the A$_{1g}$ phonon that is sensitive to the radial strain component, there is a nonlinear trend of firstly increase and then decrease from edge to center. The shift rate of A$_{1g}$ Raman mode with total in-plane strain was further measured. For WS$_2$, the value of $f(v)$ is 0.729.

Thus, the total in-plane strain could be expressed as $\varepsilon_p^{bottom} = 1.458(\frac{H_{max}}{R})^2$. Figure S3e

presents the peak position of A$_{1g}$ modes as a function of the total in-plane strain (ε_p). The peak position of the A$_{1g}$ mode shifted linearly with strain at a rate of - 1.6 cm^{-1}/%. According to the shift rate of peak position of A$_{1g}$ mode with strain, the total in-plane strain distribution along hole diameter in Figure S3f could be obtained. The total in-plane strain presents a nonlinear trend from

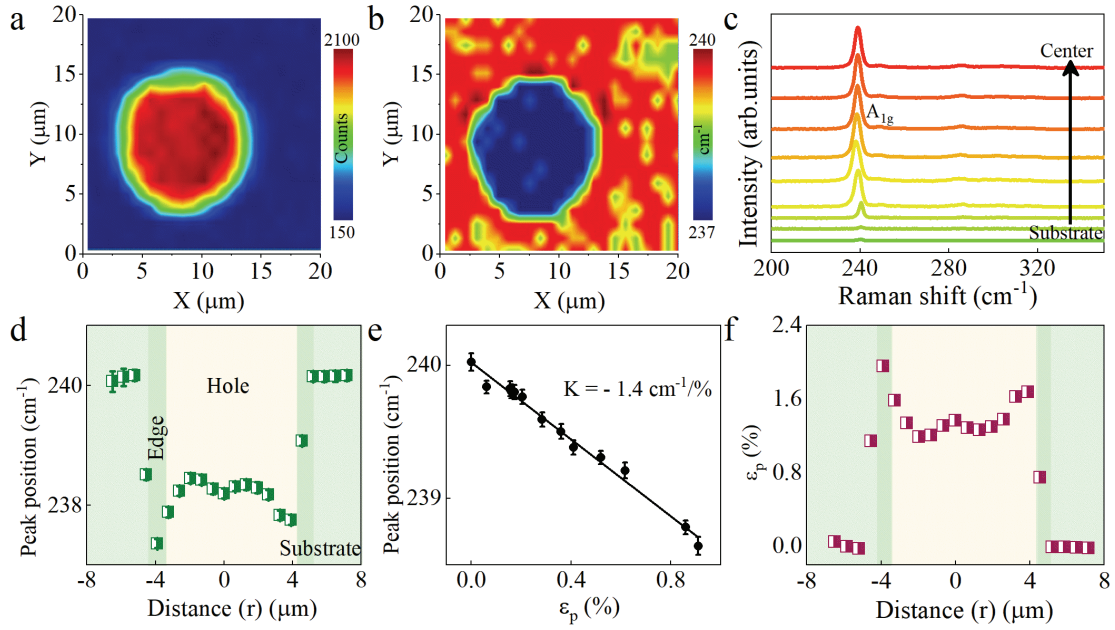edge to center, decreasing first and then increasing.

Figure S4 | The Raman spectroscopy measurements of monolayer bent MoSe₂ flakes. The A_{1g} Raman mode **(a)** intensity and **(b)** peak position mapping images of a suspended monolayer MoSe₂. **(c)** A series of Raman spectra from the center to the substrate along diameter of hole. **(d)** Raman peak positions of A_{1g} mode as functions of r. **(e)** Raman peak position of A_{1g} as a function of biaxial strain. The black solid line is obtained by the least square fitting, and the fitted slope is $K = -1.4$ cm⁻¹ /%. **(f)** The strain distribution as functions of r.

The E_{2g} and A_{1g} mode of monolayer MoSe₂ films are located at 240.6 cm⁻¹ and 290 cm⁻¹, respectively. [3] The most prominent peak A_{1g} is around 240 cm⁻¹, which is induced by out of plane vibration. Taking the monolayer MoSe₂ membrane with the bending depth of 486.02 nm (the hole diameter is 5.24 μm) as an example, the distribution of strain along the hole diameter was presented. Figure S4a-b display the intensity and peak position mapping images around the bands of A_{1g} mode. Similarly, the existence of local non-uniform strain induces the A_{1g} phonon to soften continuously from the edge to the center. Figure S4c presents Raman spectra of MoSe₂ flakes from substrate to center. In addition, the Raman frequency (peak position) of A_{1g} as a function of r was shown in Figure S4d. Since the A_{1g} phonon is more sensitive to the radial strain component, there is a nonlinear trend of firstly increase and then decrease from edge to center. To further quantify the distribution of ε_p, the shift rate of A_{1g} Raman mode with total in-plane strain was measured. For MoSe₂, the value of $f(v)$ is 0.725. Thus, the total in-plane strain could be expressed as

$$\varepsilon_p^{bottom} = 1.45(\frac{H_{max}}{R})^2.$$ Figure S4e presents the peak position of A_{1g} modes as a function of the

total in-plane strain (ε_p). The peak position of the A_{1g} mode shifted linearly with strain at a rate of - 1.4 cm⁻¹/%. According to the shift rate of peak position of A_{1g} mode with strain, the total in-plane strain distribution along hole diameter in Figure S4f could be obtained. The total in-plane strain presents a nonlinear trend from edge to center, decreasing first and then increasing.
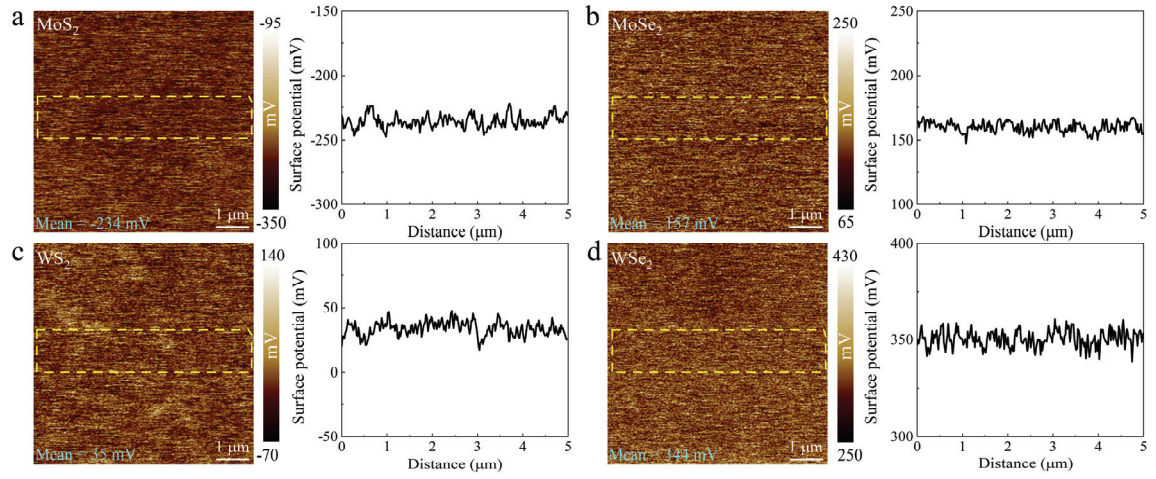
Figure S5 | The surface potential measurements of MX$_2$ (M = Mo, W; X = S, Se) flakes. The surface potential of monolayer **(a)** MoS$_2$, **(b)** MoSe$_2$, **(c)** WS$_2$, and **(d)** WSe$_2$ flakes. The surface potential distribution plotted along the yellow rectangular box is shown on the right.
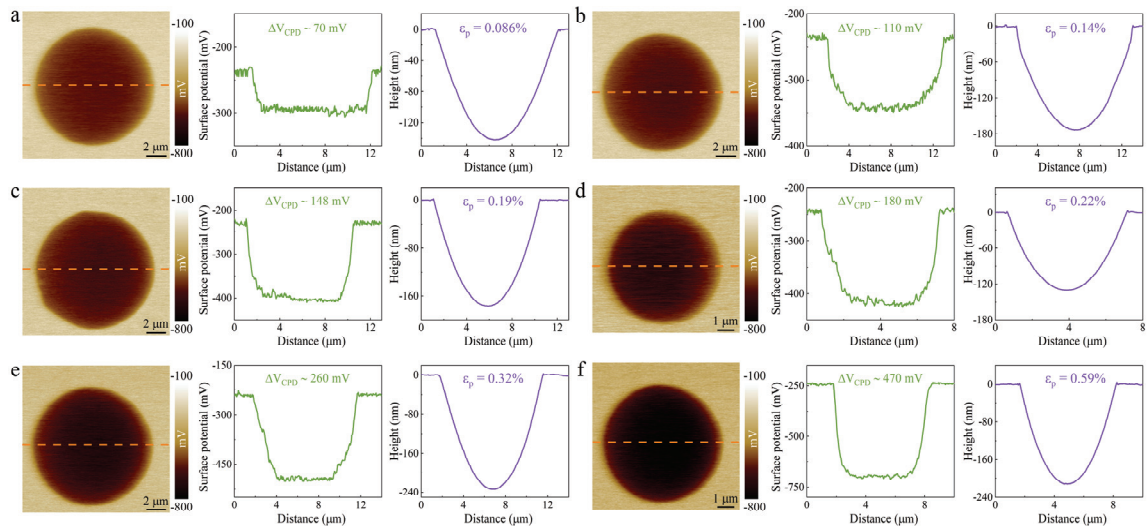
Figure S6 | The surface potential measurements of monolayer MoS₂ with various bending states. The surface potential and AFM topography plotted along the orange dashed line are shown on the right.

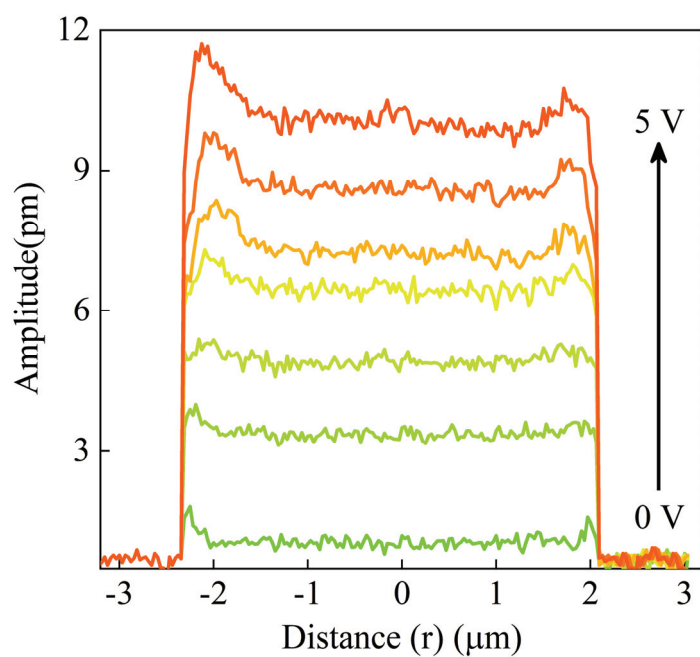**Supplementary Note 2: The out-of-plane piezoelectric response amplitude of curved monolayer MoS$_2$**

Figure S7 | The out-of-plane piezoelectric response amplitude of the monolayer MoS$_2$ curved film along diameter of hole under different driving voltages.

The piezoelectric response of the curved area is much stronger than that of the flat area. Compared with flat regions, the piezoelectric response of suspended areas increases linearly with the driving voltage. This phenomenon indicates the existence of flexoelectricity in curved films.
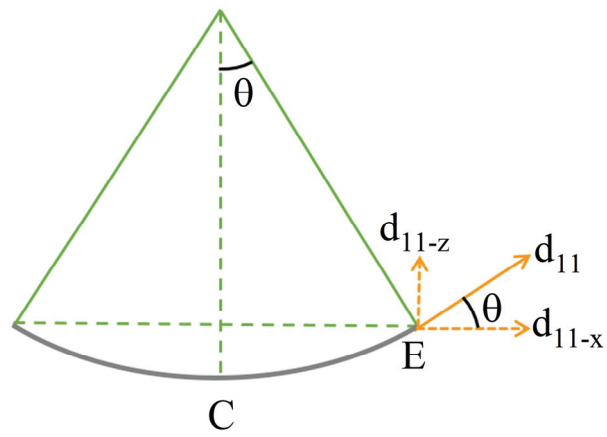
Figure S8 | The projection of intrinsic in-plane piezoelectric coefficient of bent 2D materials.

Supplementary Note 3: The calculation method and specific values of $\frac{\partial \varepsilon_p}{\partial z}$

Taking monolayer MoS$_2$ flakes as an example, the calculation method and specific values of $\frac{\partial \varepsilon_p}{\partial z}$ is shown. R is the hole radius. The radial coordinate along the hole diameter is defined as r. At the center of the hole, r is defined as zero. From the center to the edge, the total in-plane strain corresponding to each r is obtained from Figure 4f, as shown in the Table S1. Z is the bending depth of the monolayer MoS$_2$ membrane. At the hole center, define $z = 0$. From the scanning height map of the monolayer bent MoS$_2$ film along diameter of hole, the value of z corresponding to each r could be obtained. The relationship between ε_p and z is obtained by curve fitting. When -2.025 < r < -1.012, ε_p = 0.0038z – 0.53. At this time, the strain gradient of the total in-plane strain along the z-axis is 0.0038 %/nm. When r ranges from 0 to -1.012, $\partial \varepsilon_p / \partial z$ = - 0.0032.

Table S1. The specific values of $\frac{\partial \varepsilon_p}{\partial z}$

r/R	r (μm)	z (nm)	ε_p(%)	Fitting relationship between ε_p and z	$\partial \varepsilon_p / \partial z$ (%/nm)
-0.858	-2.025	108.671	-0.126		
-0.715	-1.687	67.088	-0.241	ε_p = 0.0038z – 0.53	0.0038
-0.572	-1.349	40.059	-0.404		
-0.429	-1.012	23.425	-0.433		
-0.286	-0.675	11.228	-0.404		
-0.143	-0.337	2.218	-0.375	ε_p = -0.0032z – 0.36	-0.0032
0	0	0	-0.353		

Supplementary Note 4: The distribution of d_{33}^{eff} coefficients along hole diameter in monolayer MX$_2$ (M = Mo, W; X = S, Se) films

For monolayer WSe$_2$, WS$_2$, and MoSe$_2$ flakes, the fluctuation of d_{33}^{eff} coefficients present a strong correlation with the distribution of ε_p.
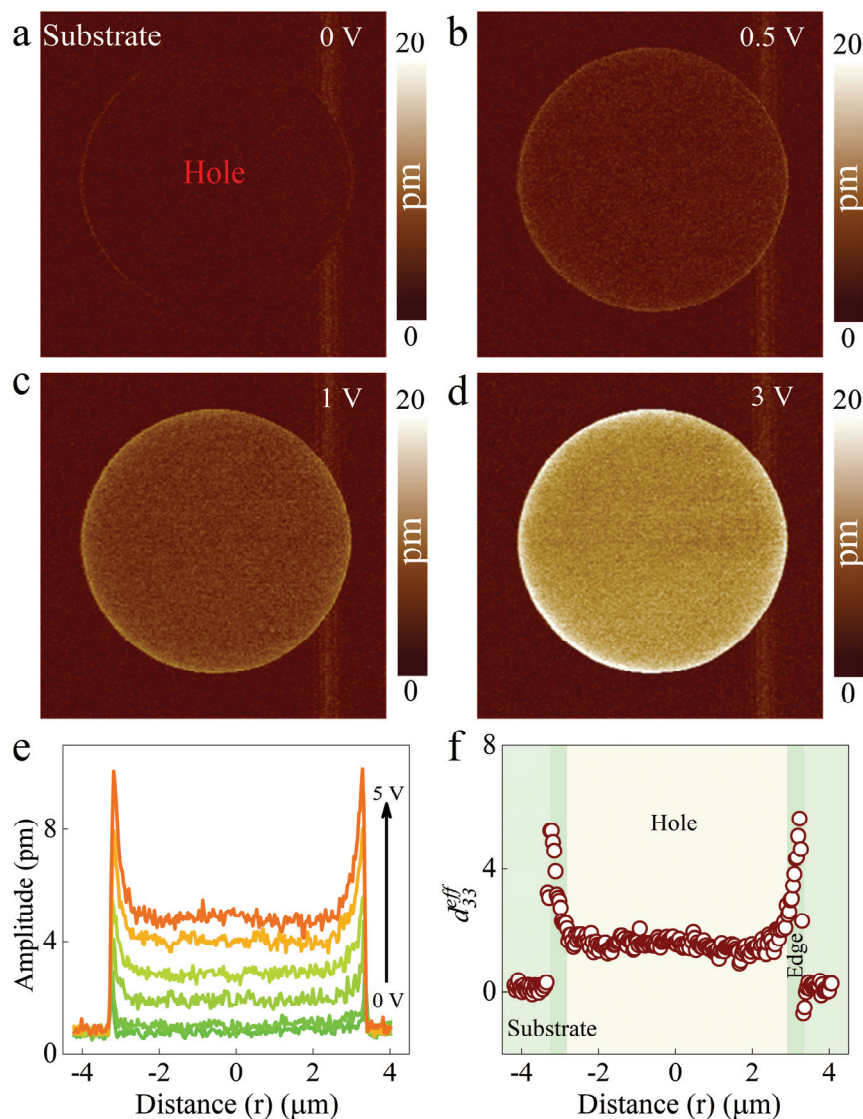

Figure S9 | PFM characterization of monolayer suspended WSe$_2$ films. Out-of-plane piezoresponse amplitude images of monolayer WSe$_2$ under the driving voltage of **(a)** 0 V, **(b)** 0.5 V, **(c)** 1 V, and **(d)** 3 V, respectively. **(e)** The out-of-plane piezoelectric response amplitude of the monolayer WSe$_2$ curved film along diameter of hole under different driving voltages. **(f)** d_{33}^{eff}-coefficients along the hole diameter as a function of r.

Figure S9a-d present the out-of-plane piezoelectric response images of the monolayer WSe$_2$ corresponding to Figure S2 under the various driving voltages. Due to the existence of the flexoelectric effect in bending regions, there is a distinct piezoresponse amplitude variation between the curved and flat WSe$_2$ membrane under non-zero driving voltage. The out-of-plane piezoelectric response amplitude of the monolayer WSe$_2$ curved film along diameter of hole under

different driving voltages was shown in Figure S9e. Compared with the flat area, the piezoelectric response of the curved area is much stronger and increases linearly with the driving voltage. This phenomenon indicates the existence of flexoelectricity in curved WSe$_2$ films. d_{33}^{eff}- coefficients along the hole diameter were plotted as a function of r in Figure S9f. For the monolayer WSe$_2$ membrane with the bending depth of 243.23 nm (the hole diameter is 3.2 μm), the strain gradient is 0.005%/nm. The ε_p distribution of monolayer WSe$_2$ is shown in Figure S2f. The steep morphology at the hole edge induces a large strain, resulting in an abrupt increase of d_{33}^{eff} coefficient. At the hole center, the d_{33}^{eff} coefficient remains almost constant due to the ε_p only fluctuates in a small range.
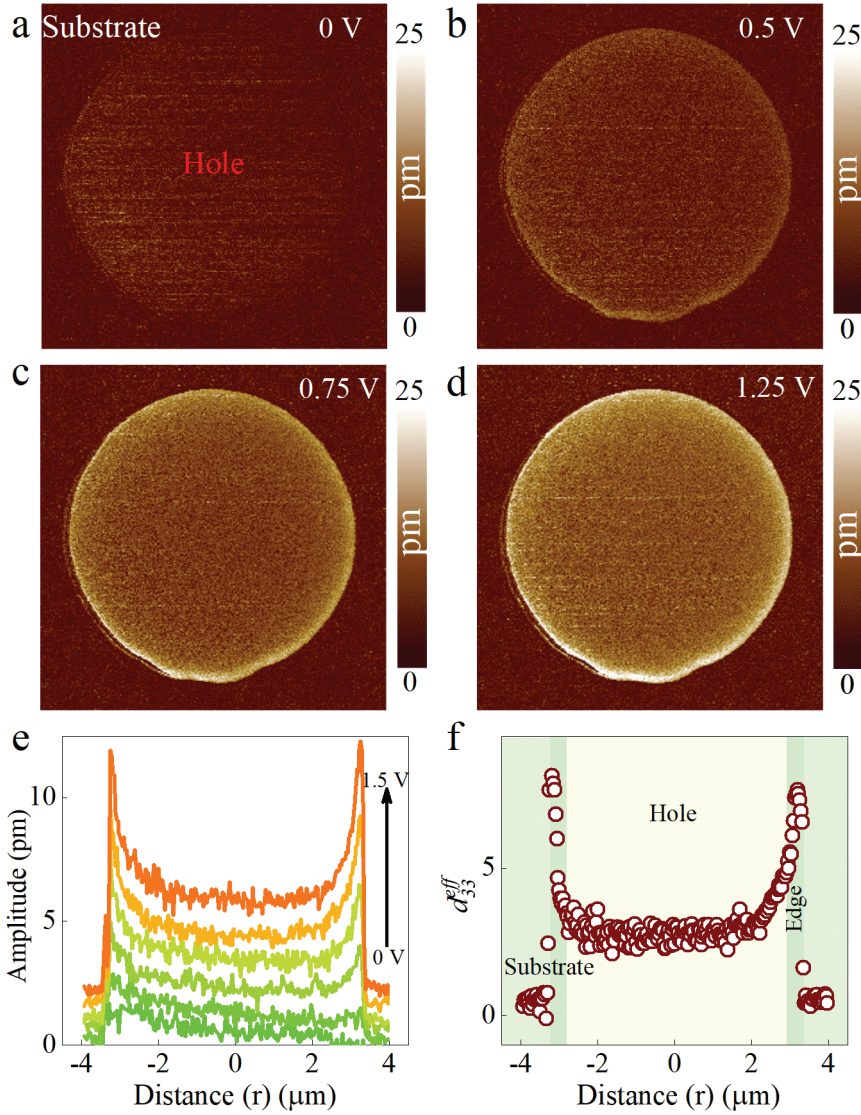
Figure S10 | PFM characterization of monolayer suspended WS₂ films. Out-of-plane piezoresponse amplitude images of monolayer WS$_2$ under the driving voltage of **(a)** 0 V, **(b)** 0.5 V, **(c)** 0.75 V, and **(d)** 1.25 V, respectively. **(e)** The out-of-plane piezoelectric response amplitude of the monolayer WS$_2$ curved film along diameter of hole under different driving voltages. **(f)** d_{33}^{eff}-coefficients along the hole diameter as a function of r.

The piezoresponse amplitude images were collected on monolayer WS$_2$ corresponding to Figure S3 under different drive voltages as presented in Figure S10a-d. When an effect modulation voltage is given, the conspicuous piezoelectric amplitude response is observed at the bent regions of monolayer WS$_2$ flakes. Note that the piezoresponse of curved WS$_2$ films is much stronger than that of flat areas. Figure S10e displays the out-of-plane piezoelectric response amplitude of the monolayer WS$_2$ curved film along diameter of hole under different driving voltages. Compared with the curved area, the piezoelectric response of the flat area is much weaker and remains unchanged with the driving voltage. d_{33}^{eff}- coefficients along the hole diameter were plotted as a function of r in Figure S10f. For the monolayer WS$_2$ membrane with the bending depth of 162.45 nm (the hole diameter is 3.4 μm), the strain gradient is 0.003%/nm. The ε_p distribution of monolayer WS$_2$ are presented in Figure S3f. The abrupt increase of d_{33}^{eff} coefficient at hole edge

is attributed to the steep morphology. Since the ε_p only fluctuates in a small range, the d_{33}^{eff} coefficient of the suspended area remains almost unchanged.
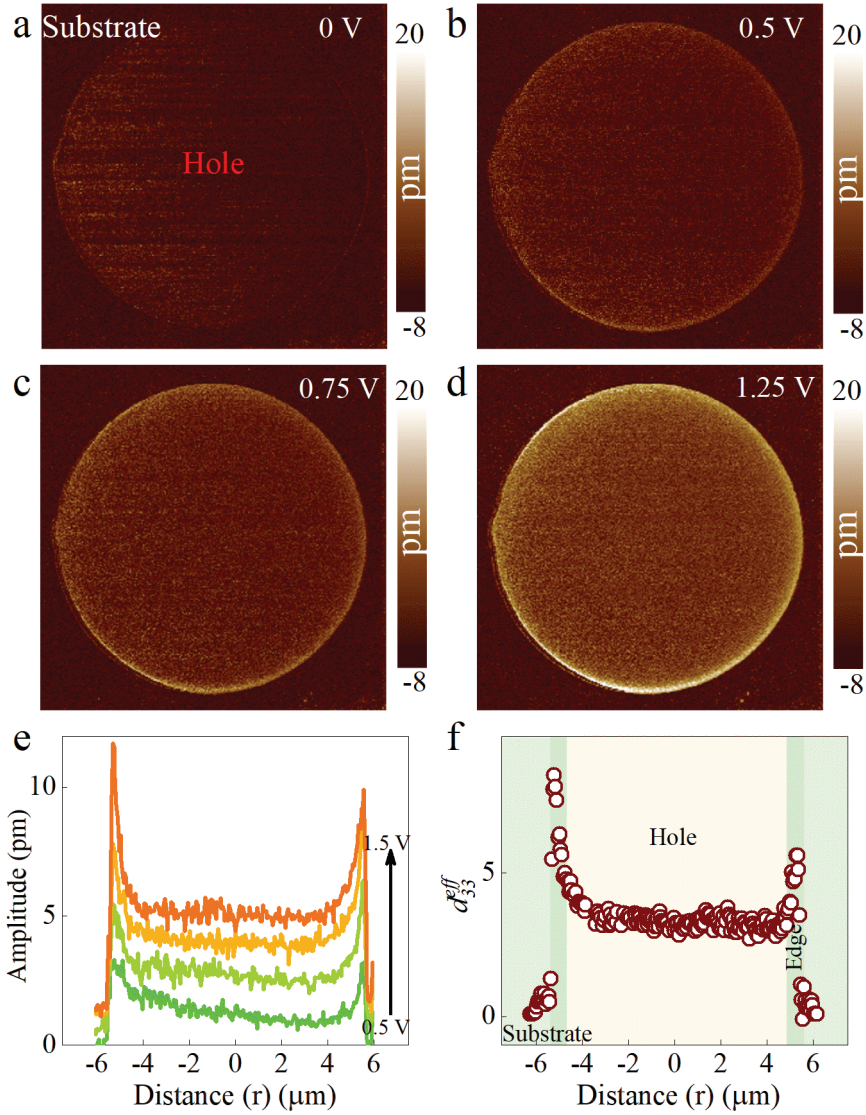
Figure S11 | PFM characterization of monolayer suspended MoSe₂ films. Out-of-plane piezoresponse amplitude images of monolayer MoSe₂ under the driving voltage of **(a)** 0 V, **(b)** 0.5 V, **(c)** 0.75 V, and **(d)** 1.25 V, respectively. **(e)** The out-of-plane piezoelectric response amplitude of the monolayer MoSe₂ curved film along diameter of hole under different driving voltages. **(f)** d_{33}^{eff} - coefficients along the hole diameter as a function of r.

Figure S11a-d displays the out-of-plane piezoresponse amplitude images of monolayer MoSe₂ corresponding to Figure S4 under the driving voltage of 0 V, 0.5 V, 0.75 V, and 1.25 V, respectively. Similarly, the piezoresponse of suspended MoSe₂ films is much stronger than that of flat areas and increases linearly with the driving voltage, as shown in Figure S11e. Meanwhile, d_{33}^{eff} - coefficients along the hole diameter were plotted as a function of r in Figure S11f. For the monolayer MoSe₂ membrane with the bending depth of 486.02 nm (the hole diameter is 5.24 μm), the strain gradient is 0.0036%/nm. The ε_p distribution of monolayer MoSe₂ are shown in Figure S4f. The fluctuation of d_{33}^{eff} coefficients is closely related to the distribution of ε_p.

Supplementary Note 5: Basic microscopic of few-layer MX$_2$ (M=Mo, W; X=Se, S) flakes
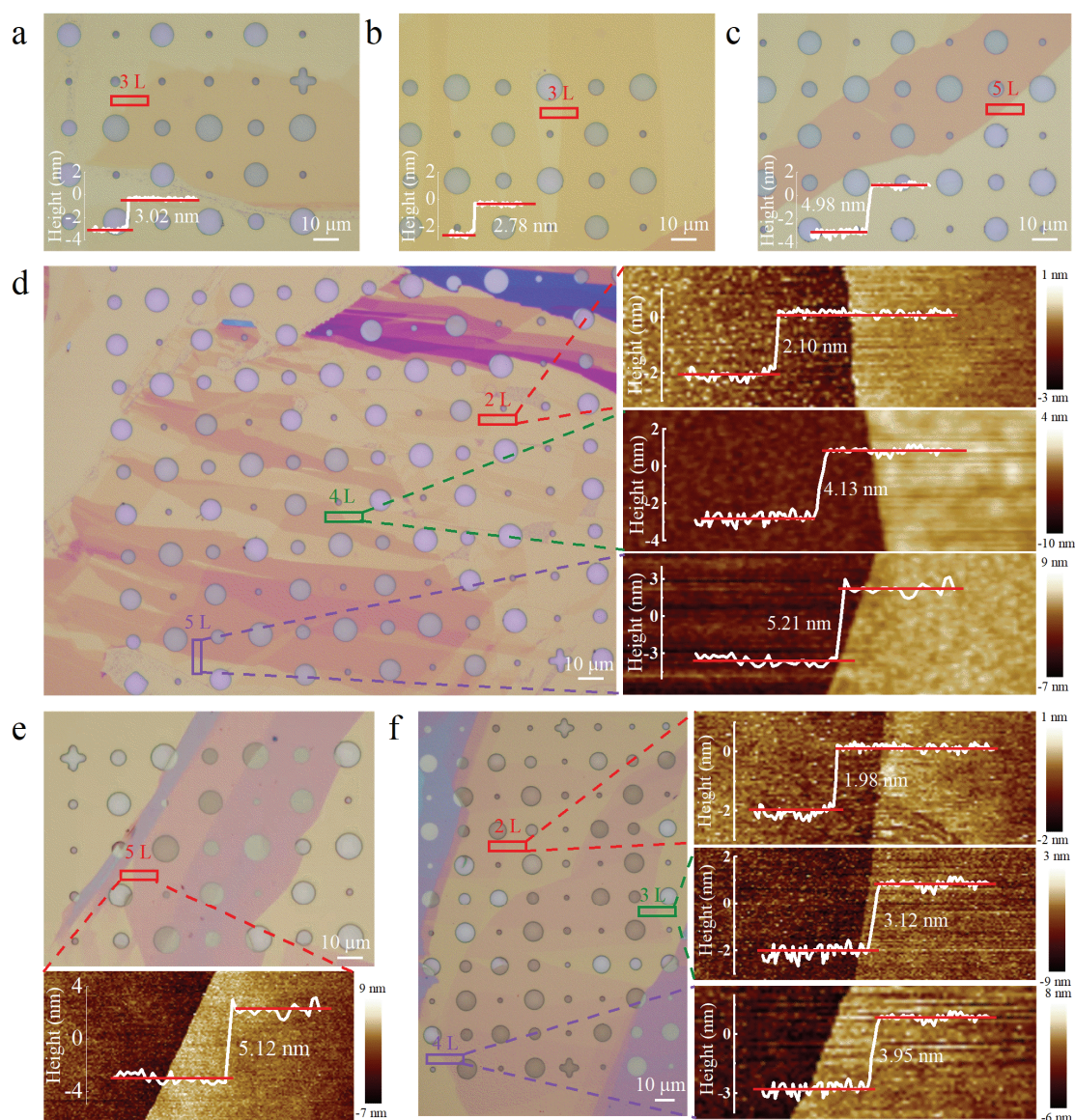

Figure S12 | Optical and AFM images of few-layered MX$_2$ flakes suspended on the porous substrates. The optical microscopy images of **(a)** 3 L MoS$_2$ flakes, **(b)** 3 L and **(c)** 5 L WSe$_2$ flakes upon the perforated substrates. Height profile along the red frame is shown in the insert. **(d)** are optical microscopy images and AFM topographic maps of 2 L, 4 L, and 5 L WS$_2$ flakes, respectively. The insets are height profiles across boundary between samples and substrates. The thickness of 2 L, 4 L, and 5 L WS$_2$ flakes are 2.10 nm, 4.13 nm, and 5.21 nm obtained from the height profiles. **(e) - (f)** are optical microscopy images and AFM topographic maps of 2 L, 3 L, 4 L, and 5 L MoSe$_2$ flakes, respectively. The insets are height profiles along the red frame.

Supplementary Note 6: Optical and AFM images of few-layered WSe₂ flakes suspended on the porous substrates
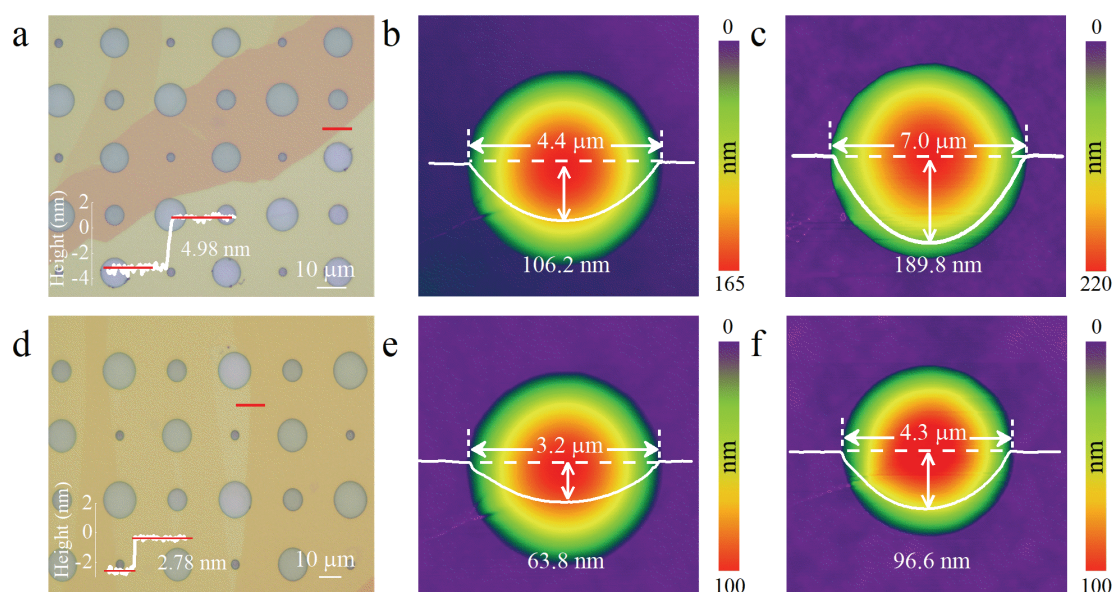

Figure S13 | The optical microscope images of WSe₂ films on perforated substrates were shown in (a) and (d). The insets are AFM topography maps of WSe₂ films with the thickness of **(a)** 4.98 nm, and **(d)** 2.78 nm. The AFM topographies of WSe₂ membranes under diverse bending states are shown in **(b) - (c)** and **(e) - (f)**. Scan height maps along diameter of hole were shown in the inset.

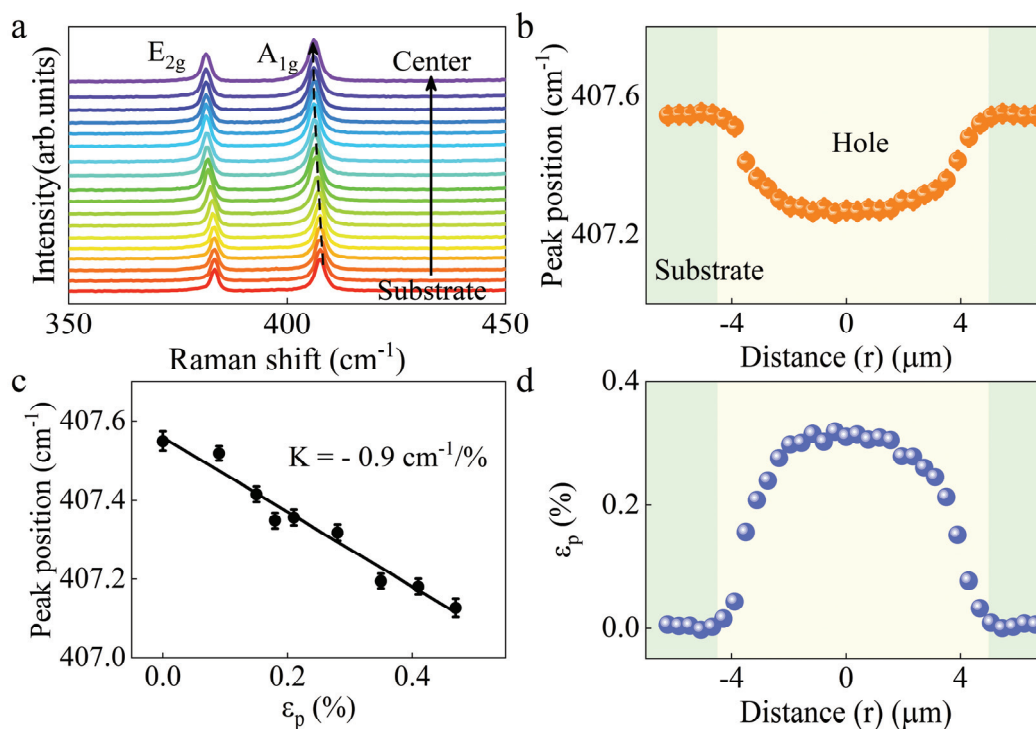**Supplementary Note 7: Nonuniform strain quantification of thin-layered MoS$_2$, WS$_2$, and MoSe$_2$ membranes**

Figure S14 | The Raman spectroscopy measurements of few-layered bent MoS$_2$ membranes. **(a)** Raman spectra of 3 L MoS$_2$ fakes from the edge to the center along diameter of hole. **(b)** Raman peak position of A$_{1g}$ as a function of r. The center of bent MoS$_2$ film is defined as r=0. **(c)** Raman peak position of A$_{1g}$ as a function of biaxial strain. The black solid line is obtained by the least square fitting, and the fitted slope is K= - 0.9 cm^{-1}/%. **(d)** The strain distribution diagram corresponding to the peak position distribution in panel (b).

Taking the 3 L MoS$_2$ membrane with the bending depth of 260.07 nm (the hole diameter is 5.60 µm) as an example, the Raman spectra from the edge to the center along the hole diameter were presented in Figure S14a. The peak position decreases nonlinearly from edge to hole center, presenting a centrally symmetric distribution, as shown in Figure S14b. For MoS$_2$, the ν value of 0.249, and then $f(v)$ = 0.721. Thus, the total in-plane strain at the center of MoS$_2$ flakes could be further obtained. Raman spectra at the center of MoS$_2$ flakes with diverse diameters and the different bending depths were measured. Figure S14c displays the peak position of A$_{1g}$ modes as a function of the ε_p. The peak position of A$_{1g}$ mode shifted linearly with strain at a rate of - 0.9 cm^{-1}/%. According to the shift rate of peak position of A$_{1g}$ mode with strain, the strain distribution of thin-layered suspended films could be obtained by the peak position distribution in Figure S14b. The total in-plane strain distribution along diameter of hole was shown in Figure S14d. The total in-plane strain reaches the maximum value of 0.31 % at the hole center, presenting a central-symmetric distribution. This result is consistent with the strain distribution of few-layered WSe$_2$ films.
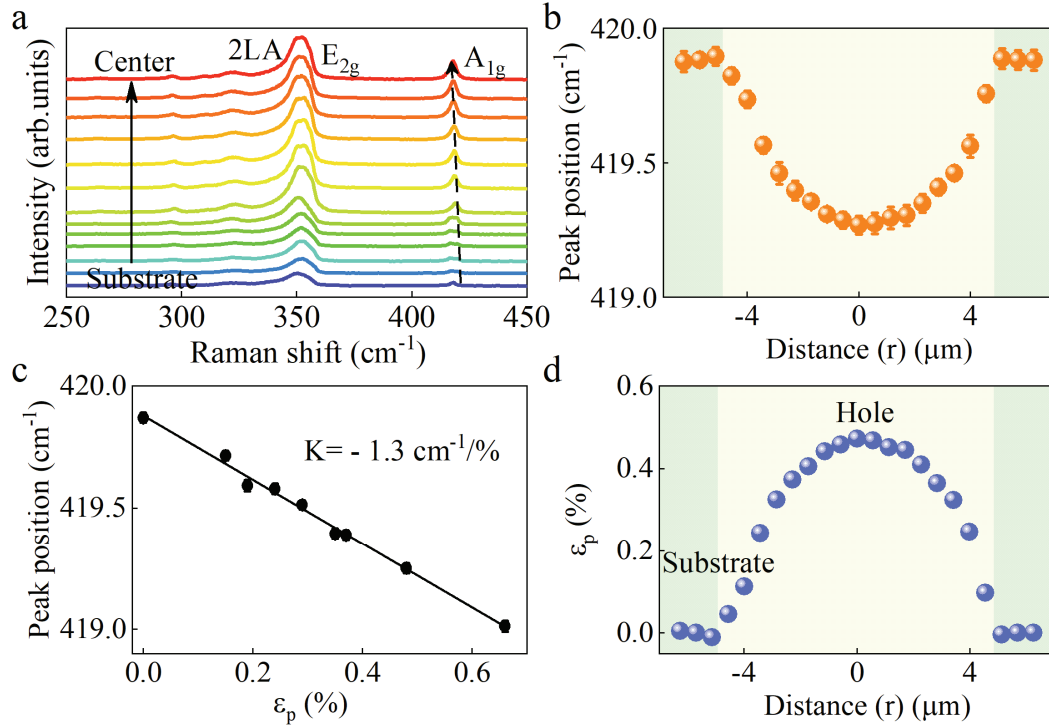
Figure S15 | The Raman spectroscopy measurements of few-layered bent WS$_2$ membranes.
(a) Raman spectra of 2 L WS$_2$ membranes from the edge to the center along diameter of hole. **(b)** Raman peak position of A$_{1g}$ as a function of r. The center of bent WS$_2$ film is defined as r=0. **(c)** Raman peak position of A$_{1g}$ as a function of biaxial strain. The black solid line is obtained by the least square fitting, and the fitted slope is K= - 1.3 cm^{-1}/%. **(d)** The strain distribution diagram corresponding to the peak position distribution in panel (b).

Taking the 2 L WS$_2$ flake with the bending depth of 290.58 nm (the hole diameter is 5.13 μm) as an example, the Raman spectra from the edge to the center along the hole diameter were shown in Figure S15a. Figure S15b displays the peak position from edge to hole center. The peak position decreases nonlinearly and presents a centrally symmetric distribution. For WS$_2$, the ν value of 0.217, and then $f(\nu)$ = 0.729. Thus, the total in-plane strain at the center of WS$_2$ flakes could be further obtained. Similarly, Raman spectra at the center of WS$_2$ flakes with diverse diameters and the various bending depths were measured. The peak position of A$_{1g}$ modes as a function of the ε_p were presented in Figure S15c. The peak position of A$_{1g}$ mode shifted linearly with strain at a rate of − 1.3 cm^{-1}/%. The strain distribution of thin-layered suspended films could be obtained according to the shift rate of peak position of A$_{1g}$ mode with strain. The total in-plane strain distribution along diameter of hole was shown in Figure S15d. The total in-plane strain reaches the maximum value of 0.47 % at the hole center, presenting a central-symmetric distribution.
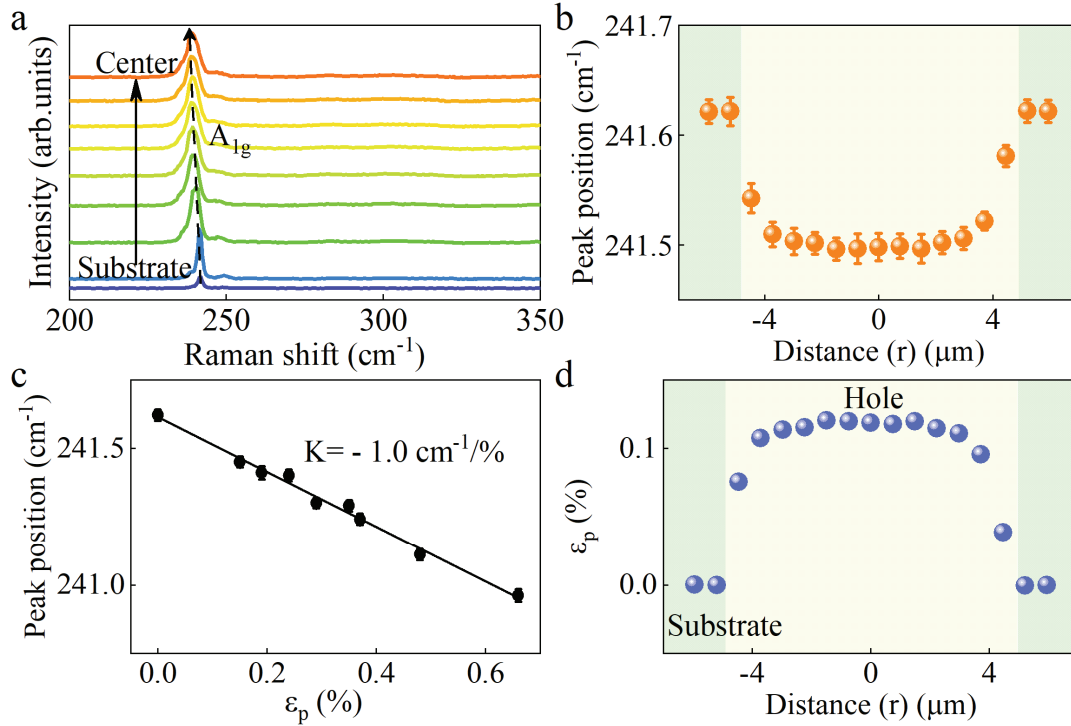
Figure S16 | The Raman spectroscopy measurements of few-layered bent MoSe$_2$ membranes.
(a) Raman spectra of 3 L MoSe$_2$ membranes from the edge to the center along diameter of hole. **(b)** Raman peak position of A$_{1g}$ as a function of r. The center of bent MoSe$_2$ film is defined as r=0. **(c)** Raman peak position of A$_{1g}$ as a function of biaxial strain. The black solid line is obtained by the least square fitting, and the fitted slope is K= - 1.0 cm^{-1}/%. **(d)** The strain distribution diagram corresponding to the peak position distribution in panel (b).

The Raman spectra of the 3 L MoSe$_2$ flake with the bending depth of 154.08 nm (the hole diameter is 5.20 μm) from the edge to the center along the hole diameter were displayed in Figure S16a. We extracted Raman frequency (peak position) of A$_{1g}$ as a function of r, as shown in Figure S16b. Similarly, the peak position reaches the minimum value at the hole center, presenting a central-symmetric distribution. For MoSe$_2$, the ν value of 0.239, and then $f(\nu) = 0.725$. Thus, the total in-plane strain at the center of MoSe$_2$ flakes could be further obtained. The peak position of A$_{1g}$ modes as a function of the ε_p, like those in Figure S16c. The peak position of A$_{1g}$ mode shifted linearly with strain at a rate of − 1.0 cm^{-1}/%. According to the shift rate of peak position of A$_{1g}$ mode with strain, the strain distribution of thin-layered MoSe$_2$ films could be obtained. Figure S16d presents the total in-plane strain distribution along diameter of hole. The ε_p increases nonlinearly and presents a centrally symmetric distribution.

Supplementary Note 8: PFM characterization of few-layered suspended WSe₂ films
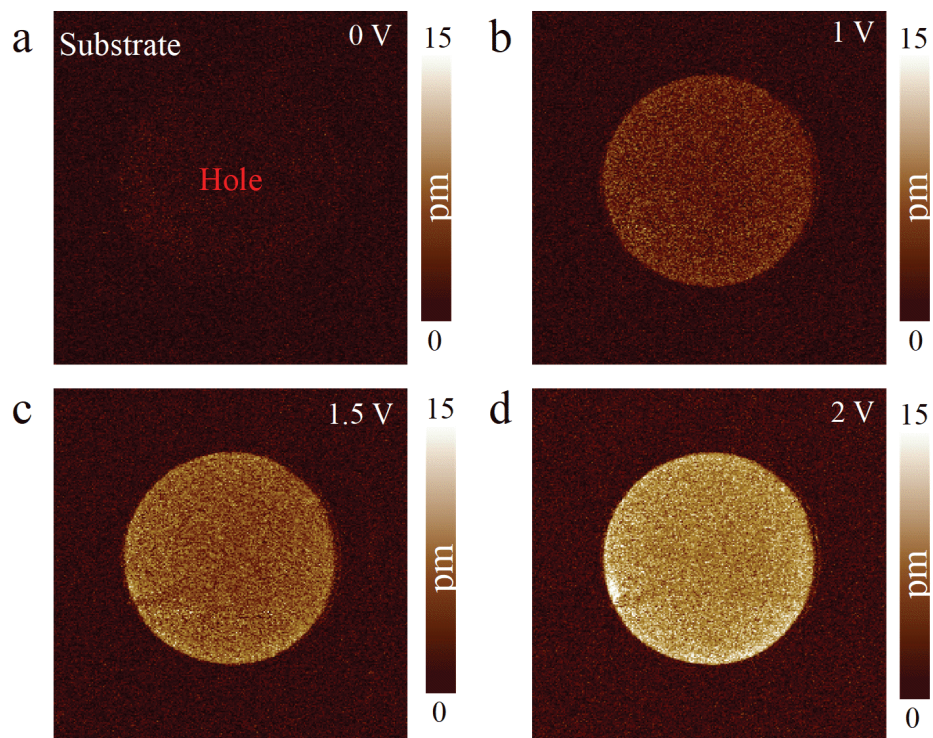

Figure S17 | PFM characterization of few-layered suspended WSe₂ films. The out-of-plane piezoelectric response image of WSe₂ flakes with thickness of 4.23 nm under the driving voltage of **(a)** 0 V, **(b)** 1 V, **(c)** 1.5 V and **(d)** 2 V.

Supplementary Note 9: The elastic coefficient of suspended MX2 (M = Mo, W; X = S, Se) films

Table S2. The elastic coefficient of MX_2 (M = Mo, W; X = S, Se) flakes [4]

Materials	Number of layers	c_{11} [GPa]
WS$_2$	1	272±18
	3-8	236±65
WSe$_2$	5-12	167±7
	4-9	163±39
MoSe$_2$	1-2	177.2±9.3
	5-10	224±41
MoS$_2$	1	265±13
	3-11	246±35

References

1. A. M. Dadgar, D. Scullion, K. Kang, D. Esposito, E. H. Yang, I. P. Herman, M. A. Pimenta, E. J. G. Santos, and A. N. Pasupathy, *Chem. Mater.*, 2018, **30**, 5148.

2. C. Cong, J. Shang, X. Wu, B. Cao, N. Peimyoo, C. Qiu, L. Sun, and T. Yu, *Adv. Opt. Mater.*, 2014, **2**, 131.

3. X. Lu, M. I. B. Utama, J. Lin, X. Gong, J. Zhang, Y. Y. Zhao, S. T. Pantelides, J. X. Wang, Z. L. Dong, Z. Liu, W. Zhou, and Q. Xiong, *Nano Lett.*, 2014, **14**, 2419.

4. N, Iguiñiz, R. Frisenda, R. Bratschitsch, and A. Castellanos-Gomez, *Adv. Mater.*, 2019, **31**, 1807150.